Sensitive Photodetector Arrays Based on Patterned CH₃NH₃PbBr₃ Single Crystal Microplate for Image Sensing Application

Chen Li, Jia-Xiang Li, Chun-Yan Li, Jiang Wang, Xiao-Wei Tong, Zhi-Xiang Zhang, Zhi-Ping Yin,* Di Wu, and Lin-Bao Luo*

Hybrid perovskite has attracted intensive attention for its diverse optoelectronic applications, and integrated perovskite devices are broadly required in various functional optoelectronics. In this study, an integrated photodetector (PD) array is developed based on perovskite microplate arrays for trajectory track and image sensing application. The perovskite microplate array is fabricated by a modified photolithography method, which can confine the growth of perovskite single-crystal microplate arrays with controlled dimension. Optoelectronic measurement of the microplate array device reveals that the as-fabricated PD devices exhibit not only obvious photoresponse characteristics at zero bias, with a high on–off ratio of up to 1.5×10^4, a responsivity of 0.38 AW^{-1}, and specific detectivity of 1.7×10^{12} Jones, respectively, but also relatively good uniformity, with neglectable pixel-to-pixel variation. In addition, the as-integrated PD arrays can capture real-time light traces and record simple character with satisfactory resolution, which indicates that the current integrated perovskite device has potential application in light trajectory tracking and image sensing.

1. Introduction

Owing to their amazing optoelectronic properties (e.g., low trap density,[1,2] high carrier mobility, and tunable bandgap[3]), organic–inorganic hybrid perovskite materials have become promising candidates for diverse optoelectronic applications including solar cells,[4–6] light emitting diodes,[7] low-threshold lasers,[8] and photodetectors (PDs).[9–11] For example, by confined growth of perovskite single-crystal film,[12] Yang and co-workers have achieved the controlled fabrication of high-quality ultrathin MAPbBr₃ film, which have low trap density, high carrier mobility, and longer carrier diffusion length and lifetime. It is found that these the perovskite exhibits a record photoconductive gain of 50 million and a gain-bandwidth product of 70 GHz. Furthermore, by using a similar growth technique, Jing et al. have also realized a high sensitive photodetector based on ultrathin perovskite film, with a responsivity as high as 5600 AW^{-1}.[13] In spite of these progress, miniaturized and integrated optoelectronic device arrays with typical size down to micrometer or even nanometer remains highly challenging,[14–16] as controlled fabrication of high-quality perovskite microstructure arrays is still difficult.

Photolithography is the most representative technology for materials patterning and device integration in modern semiconductor industry. However, traditional photolithography technique could not be applied directly for perovskite patterning for its soluble properties in polar solvents. To date, various alternative technologies have been reported, which could be roughly divided into two types, top-down and bottom-up methods.[17] The top-down approach often involve the direct patterning processes such as laser-induced growth,[18] focused ion beam etching,[19] inkjet printing,[20] and so on. These technologies could achieve effective control over the dimension, resolution, and alignment of the perovskite arrays. Nevertheless, they often need very complicated instruments and sometimes inevitable damage may occur when illuminated by the laser or focused ion beam. On the other hand, the bottom-up method normally involves preparing templates/patterns first before perovskite growth, which have the advantages of easy processablity and versatility. Moreover, by precisely tuning the perovskite growth process in the template, improved crystal quality could be easily obtained. For this bottom-up strategy, the fixed templates of polydimethylsiloxane (PDMS) and anodic aluminum oxide are usually adopted to grow perovskite

C. Li, Prof. Z.-P. Yin
Academy of Opto-electronic Technology
Hefei University of Technology
Hefei 230009, China
E-mail: liying87@hfut.edu.cn
C. Li, J.-X. Li, C.-Y. Li, J. Wang, X.-W. Tong, Z.-X. Zhang, Prof. L.-B. Luo
School of Microelectronics
Hefei University of Technology
Hefei 230009, China
E-mail: luolb@hfut.edu.cn
Prof. Z.-P. Yin
Special Display and Imaging Technology Innovation Center
of Anhui Province
Hefei 230009, China
Dr. D. Wu
School of Physics and Microelectronics
Zhengzhou University
Zhengzhou 450052, China

The ORCID identification number(s) for the author(s) of this article can be found under https://doi.org/10.1002/adom.202100371.

ADVANCED
SCIENCE NEWS
www.advancedsciencenews.com

ADVANCED
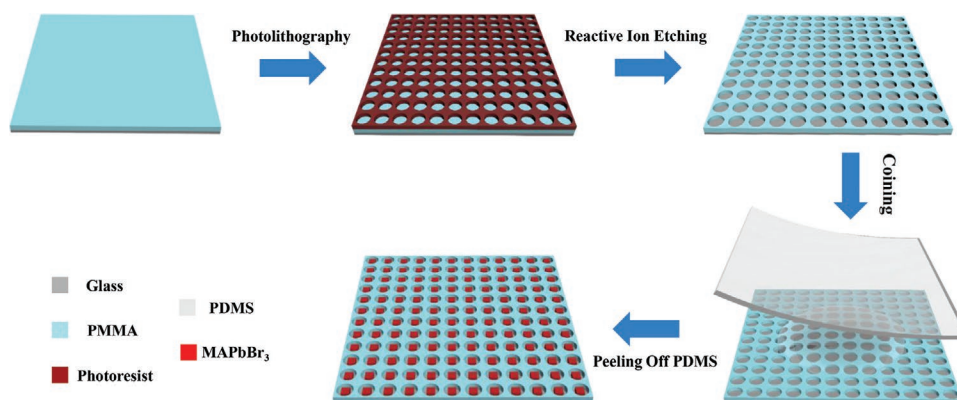**OPTICAL**
MATERIALS
www.advopticalmat.de

Figure 1. Schematic illustration of the procedures for fabricating patterned MAPbBr₃ single crystal arrays.

arrays.[21–24] Besides, the template could also be provided by a modified photolithography method,[25,26] which usually employs a new auxiliary layer in combination with the photolithography. In comparison with the fixed template, the most appealing part of the modified photolithography method lies in its high resolution, complex templates fabrication as well as excellent alignment with the patterned electrodes. For above reason, this approach possesses the high potential for large-scale perovskite device integration. For example, Gong and co-workers[27] have successfully patterned the perovskite precursor solution into arrays through a poly-TPD auxiliary layer assisted photolithography process, and then uniform $CH_3NH_3PbBr_3$ (MAPbBr₃) single crystal microarrays were achieved via an Ostwald ripening crystallization process. Furthermore, they have also achieved the construction of microarray solar cells, which exhibited enhanced performance than continuous single crystals. Moreover, Shin group[28] has demonstrated planar PD arrays composed of MAPbI₃ film, which was grown by using a photopatterned polymer template for the perovskite growth via a vapor phase conversion process. In spite of these progresses on the perovskite-related integrated devices,[15,29] the fabrication of large-scale and high-quality single-crystal perovskite arrays with desired morphology and dimension, and the precise alignment of the electrodes in the device integration process remains a challenge.

In light of the above, we herein present the controlled fabrication of MAPbBr₃ single-crystal microplates and their further application in integrated PD device array. It is found that this synthesis method is capable of growing perovskite crystals with controlled position and size. Device analysis reveals that the as-fabricated perovskite PD has typical on/off current ratio, responsivity, and specific detectivity of 1.5×10^4, 0.38 AW⁻¹, and 1.7×10^{12} Jones at zero bias, respectively, which is much better than many perovskite materials based devices. Furthermore, the dark current of 6×6 addressable PD arrays based on the perovskite microplates fluctuates from 1 to 10 pA, while their corresponding photocurrent ranges from 1 to 10 nA with neglectable pixel-to-pixel variation. It is also found that the integrated PD arrays were applied for real-time light trajectory and visible light imaging. The results demonstrate that the as-fabricated integrated devices may have prospective applications in optical imaging, digital display, and so on.

2. Results and Discussion

The single-crystalline MAPbBr₃ microplate arrays were fabricated through geometrically confined growth of perovskite on a prepatterned polymethyl methacrylate (PMMA) microhole array with a diameter of 20 μm. The schematic illustration was shown in **Figure 1**. Briefly, PMMA solution was first spin-coated on a hydrophilic glass substrate, and then the acquired PMMA thin film with a thickness of 1 μm were patterned by traditional photolithography, followed by reactive ion etching.[30] Afterward, the hydrophobic PDMS was pressed against the perovskite precursor solution on the glass substrate with a uniform pressure. In this process, the perovskite precursor solution was driven into the PMMA circular microholes array, followed by the nucleation at the edge of the circular hole after slow evaporation of the solvent.[21] Finally, the PDMS was peeled off after 6 h at room temperature, leaving rectangular MAPbBr₃ microplates, with a diameter of about 10–15 μm, according to the optical image displayed in Figure S1a,b of the Supporting Information.

Figure 2a shows the scanning electron microscope (SEM) image of the MAPbBr₃ microplate arrays. It is seen that more than 96% of the microplates are characterized by rectangular morphology, except only a few irregular ones as labeled in red circle. With the aid of the atomic force microscope (AFM), the thickness of an individual microplate was measured to be about 500 nm (Figure 2b). Further study of 60 randomly selected microplates shows that the thickness of the microplate varies from 400 to 800 nm, while length is in the range from about 10 to 15 μm, respectively (Figure S2, Supporting Information). From the energy dispersive spectrometer (EDS) profile shown in Figure 2c, the measured atomic ratio of Pb:Br:N is about 1:3:1, which is consistent with the stoichiometric value. Elemental mapping analysis reveals that the elements of Pb, Br, and N are uniformly distributed in the perovskite (Figure S3, Supporting Information). The X-ray diffraction (XRD) pattern of powder and rectangular MAPbBr₃ are shown in Figure S4 of the Supporting Information, from which a cubic crystal structure with space group *Pm-3m* can be seen.[31,32] Moreover, only {100} planes are observed in the rectangular MAPbBr₃, the peaks coincide with the MAPbBr₃ single crystal previously reported.[33] The selected area electron diffraction pattern and high-resolution transmission electron microscopy (HRTEM)
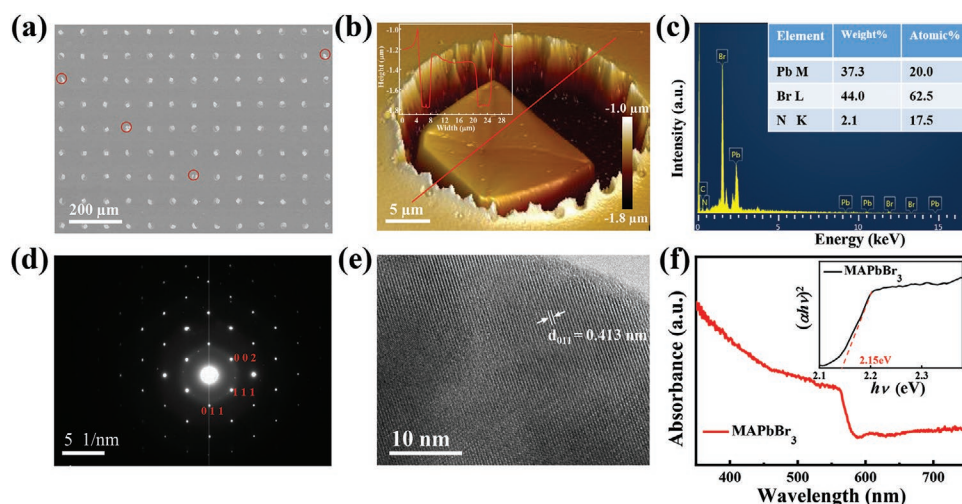
Figure 2. a) SEM image of MAPbBr$_3$ single crystal arrays, the scar bar is 200 µm. b) The corresponding AFM image, the inset in (b) shows the height profile of the perovskite single crystal. c) The EDS spectra of a MAPbBr$_3$ single crystal. d) The SEAD of MAPbBr$_3$ single crystal. e) Magnified HRTEM image of the MAPbBr$_3$ single crystal. f) Absorption and band gaps of MAPbBr$_3$ single crystal.

in Figure 2d,e further confirms the single crystal structure of the as-prepared MAPbBr$_3$ microplate. The absorption spectrum was measured in Figure 2f and obvious absorption edge at ≈570 nm could be observed. Based on the absorption curves, the bandgap could be determined through the Kubellka–Munk equation:[34] $(\alpha h\nu)^2 = A(h\nu - Eg)$, where α and $h\nu$ represent the absorption coefficient and incident photoenergy, respectively. The corresponding Tauc plot is presented in the inset of Figure 2f and the bandgap is finally estimated to be 2.15 eV, which is in accordance with the previous study.[35]

By using the as-patterned perovskite microplates as building blocks, we then assembled PDs with a typical sandwiched configuration of indium tin oxide (ITO)/perovskite single-crystal (PSC)/Au (**Figure 3**a). Detailed illustration of the device fabrication process is presented in Figure S5 of the Supporting Information, which consists of two main steps. Step 1: the fabrication of patterned microplates on the predesigned ITO interdigital

electrode; Step 2: thermal evaporation of Au electrode on top of the microplate arrays. Figure 3b illustrates the geometry of the as-constructed integrated PDs, each single pixel of which is formed at the intersection of the ITO and Au electrodes. In order to improve the reproducibility of the integrated device, individual pixel is actually composed of 3 × 3 microplates (inset of Figure 3b). The reason for such design is due to the existence of some irregular perovskite microplates from the SEM image (Figure 2a), which might malfunction if the pixel is too small in size. As shown in Figure S6 of the Supporting Information, each pixel covers an area of 300 × 300 µm^2, with the electrode spacing of 300 µm. Besides, the overall cross-section illustration of the integrated PD arrays is presented in Figure 3c, which consists of five layers, glass/ITO/PMMA/MAPbBr$_3$/Au from the bottom to the top layer. It should be pointed out that the PMMA act not only as a template, but also as the insulating layer to avoid short circuits between the top and bottom
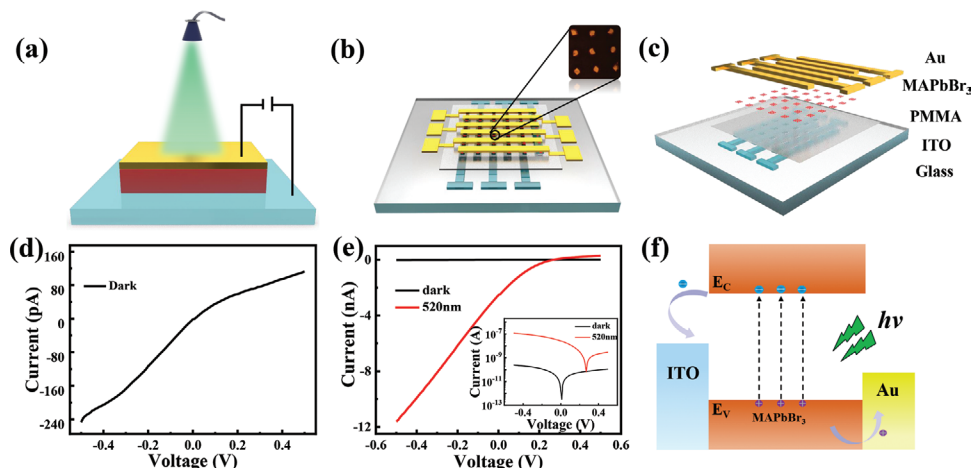

Figure 3. a) Schematic illustration of the ITO/MAPbBr$_3$ sandwiched device structure. b) The integrated photodetectors array on glass substrate, the inset is the enlarged view of one pixel in MAPbBr$_3$ optical image sensor. c) Layer-by-layer structure of MAPbBr$_3$ image sensor. d) I–V curves of the individual PD in dark. e) I–V characteristics of the device in the dark and illuminated with 520 nm. f) The energy band diagram of the single device under light illumination.

electrodes. Furthermore, the top view SEM image of the as-integrated device arrays is displayed in Figure S7 of the Supporting Information, demonstrating that the vertical PD arrays with nine microplates in each single pixel are successfully fabricated. The photoresponse characteristics of the integrated PD devices are studied. Figure 3d presents the I–V curves of an individual pixel in the dark. The nonlinear I–V characteristics suggests presence of contact barrier height, which is probably due to the surface dangling bonds or surface contamination.[36,37] When illuminated under the 520 nm light, the as-assembled device displays an apparent photovoltaic characteristics (Figure 3e), which can be understood by the energy band diagram shown in Figure 3f. Once ITO is in contact with MAPbBr$_3$, a built-in electric field with a direction pointing from ITO to the MAPbBr$_3$ could be formed due to their different in work function. As soon as the device is illuminated by the light with a higher energy than the bandgap, the photogenerated electron–hole pairs could be quickly separated by the internal electric field. Namely, the holes will move to the MAPbBr$_3$ while the electrons move to the ITO side, forming photocurrent in external circuit.

In order to elaborate on the optoelectronic performance of perovskite photodetector, the photoresponse under 520 nm illumination with different light intensities at 0 V were tested. As shown in **Figure 4**a, the channel current increases monotonously from 0.25 to 106 nA when increasing the light intensity from 0.01 to 7.46 mW cm^{-2}, which is probably due to the increased number of photogenerated charge carries under higher intensity. Moreover, the relationship between photovoltage and light intensity in Figure 4b reveals a monotonous increase in photovoltage from 119 to 267 mV with increasing light intensity. From the temporal response in Figure 4c, similar tendency was also found for the photocurrent. To further unveil the evolution of photocurrent (I) as a function of light intensity (P), the following power law is adopted (1)[38,39]

$$I_{ph} \propto P^{\theta} \tag{1}$$

where θ is an empirical exponent determined by the linear relationship of I and P. Through fitting curves with light intensity ranging from 0.01 to 7.46 mW cm^{-2}, a θ value of 0.76 is obtained (Figure 4d). It is worth noting that after storage in ambient condition for 60 days, the current device can retain nearly 90% of its initial photocurrent (Figure 4e). Such relatively good device stability can be attributed to the unique sandwich structure: The perovskite is completely wrapped by PMMA layer and two electrodes, which at a large extent slows down the degradation process. In addition, The spectral response of the perovskite PD under different wavelengths were measured in Figure S8 of the Supporting Information, the device exhibits apparent sensitivity under light from 350 to 560 nm, with a peak sensitivity at 520 nm, which is close to the bandgap of MAPbBr$_3$. The three key-figure-of-merit parameters of on/off ratio, responsivity (R) and specific detectivity (D*) were calculated by Equations (2)–(4) for the photodetector[40]

$$I_{on/off} = \frac{I_{light}}{I_{dark}} \tag{2}$$

$$R = \frac{I_{light} - I_{dark}}{P_{light}\,S} \tag{3}$$

$$D^* = \frac{R\sqrt{S}}{\sqrt{2eI_{dark}}} \tag{4}$$

where I_{light} is the photocurrent, I_{dark} is the dark current, P_{light} is the incident light power, S is the effective illumination area, and e is the elementary charge, respectively. Based on the above result, an I_{light}/I_{dark} ratio as high as 1.5×10^4 was obtained at an intensity of 7.46 mW cm^{-2}. Besides, at a weak light of 0.01 mW cm^{-2}, a high R of 0.38 AW^{-1} and D* of 1.7×10^{12} Jones are achieved (Figure 4f), respectively. From the relative balance $(V_{max} - V_{min})/V_{max}$ as a function of modulation frequency (Figure S9, Supporting Information), the 3 dB bandwidth is estimated to be 1600 Hz.
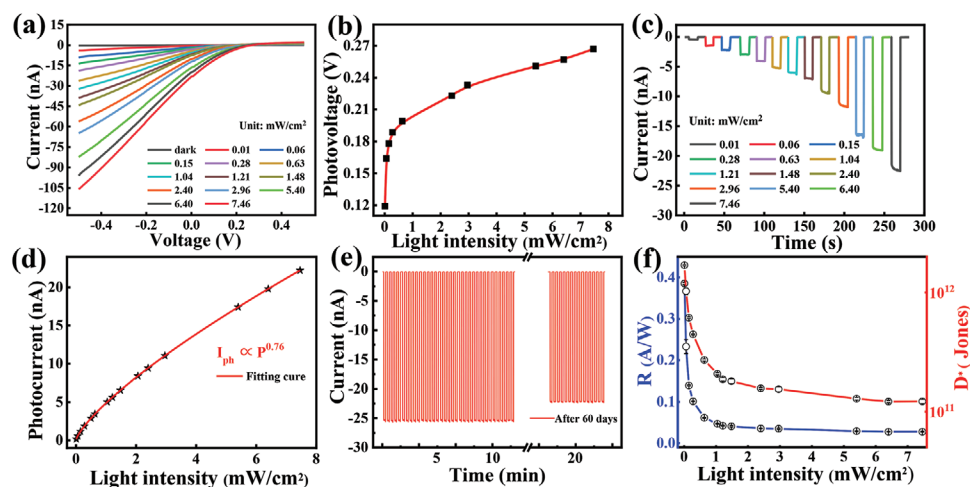

Figure 4. a) Current–voltage characteristics of the photodetector under 520 nm irradiation with varied light intensities. b) The photovoltages at various light intensities at zero bias. c) The temporal I–t responses at zero bias. d) The photocurrent as a function of the different light intensity at zero bias. e) Photoresponse of the device for 35 cycles; another 15 cycles were tested after storage in air for 60 days. f) The responsivity and specific detectivity as a function of the incident light intensity under 520 nm light at zero bias.

ADVANCED
SCIENCE NEWS
www.advancedsciencenews.com

ADVANCED
OPTICAL
MATERIALS
www.advopticalmat.de

Table 1. Summary of the performance of our device and other similar perovskite-based device.

Type	Materials	Device structure	Bias [V]	On/off	R [A W^{-1}]	Ref.
Unitary device	Bulk MAPbBr$_3$ monocrystal	Lateral	10	55	0.038	[35]
	Bulk MAPbBr$_3$ monocrystal	Lateral	4	$\approx 10^5$	16	[45]
	MAPbBr$_3$ thin film polycrystal	Vertical	−0.5	10^3	–	[41]
	MAPbI$_3$ nanowire monocrystal	Vertical	0.3	<10	0.04	[15]
	MAPbI$_{3-x}$Cl$_x$ film polycrystal	Lateral	5	1.2×10^3	2.17	[44]
Integrated devices	MAPbBr$_3$ nanowire monocrystal	Lateral	1	3.5×10^2	20	[43]
	MAPbI$_3$ microplate monocrystal	Lateral	5	$>10^3$	7	[42]
	MAPbBr$_3$ microplate monocrystal	Vertical	0	1.5×10^4	0.38	This work

Table 1 compares the main metrics of the as-assembled MAPbBr$_3$ microplate PDs and other perovskite-based device. Obviously, the values of R and D^* are higher than most of the previously reported PDs composed of polycrystalline perovskite films,[41] patterned perovskite nanowire/microplate arrays[15,42–44] and even bulk perovskite single crystal devices.[35,45] The relatively good device performance could be attributed to the following factors: 1) Relatively low dark current (10^{-12} A). In this work, the dark current is lower than most of the other perovskite based-photodetectors in the literature,[46,47] which indicates the relatively high single-crystal quality of the as-fabricated microplates. 2) The in situ growth interface between the single crystal active layer and the bottom ITO electrode, which is much better than the interface formed by spin-coating for carrier transport.[48] 3) The short transit channel. The transit distance is the thickness of the microplate for the vertical device structure, which is less than 800 nm. For this reason, the relatively short transit distance will lead

to weak recombination activity, which is highly beneficial for photodetection of the PD.[12]

To confirm the capability of the as-fabricated PDs for integrated device application, the uniformity and reliability of all pixels were then explored. First, the photodetector arrays were illuminated by a 520 nm light irradiation (2.06 mW cm^{-2}). For convenience, the photoresponse were summarized in the form of a 2D mapping with different colors to show the different currents. As shown in **Figure 5**a,b, the dark-current of all pixels fluctuates from 1 to 10 pA while their corresponding photocurrents from 1 to 10 nA, displaying relatively good uniformity. The average dark currents and photocurrents are calculated to be about 3.67 pA and 3.35 nA, respectively (Figure 5c). Besides, relatively small pixel to pixel variation was observed for both photocurrent and dark current, which is reasonable as the size and interface of PSC varies from one device to another. The I_{light}/I_{dark} ratio of all pixels were extracted and then plotted in Figure 5d. Apparently, all the individual PDs exhibit a large I_{light}/I_{dark} ratio exceeding 5×10^2.
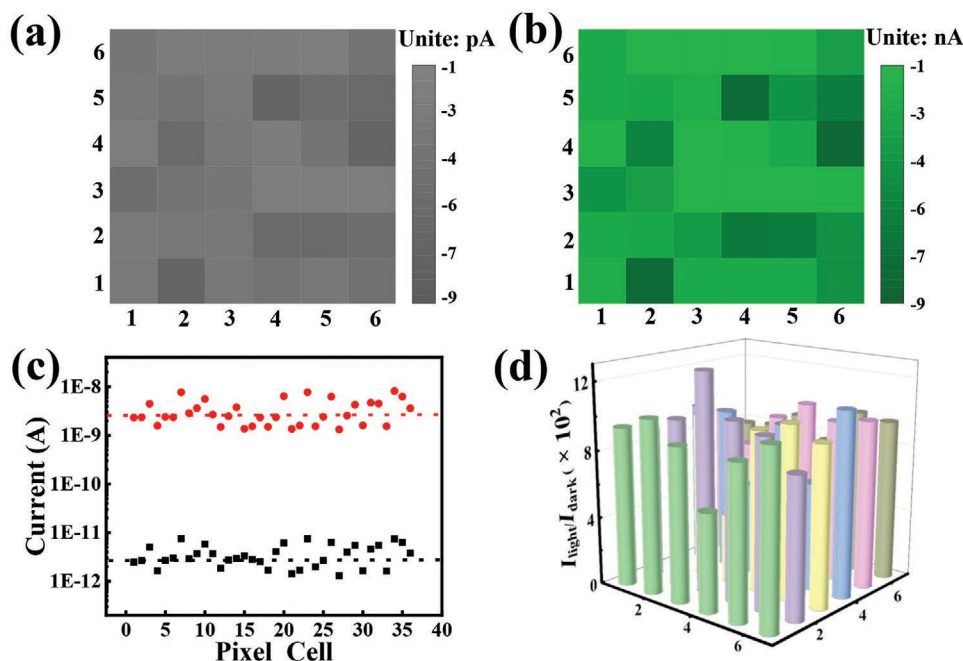

Figure 5. a) 2D contrast maps showing the channel current of photodetector arrays in dark and b) upon a homogeneous 520 nm light illumination. c) Channel current in dark and under 520 nm light illumination for each pixel device. The dashed lines represent the average values for dark current (black) and photocurrent (red). d) The 3D diagram of the I_{light}/I_{dark} ratio for each pixel device.
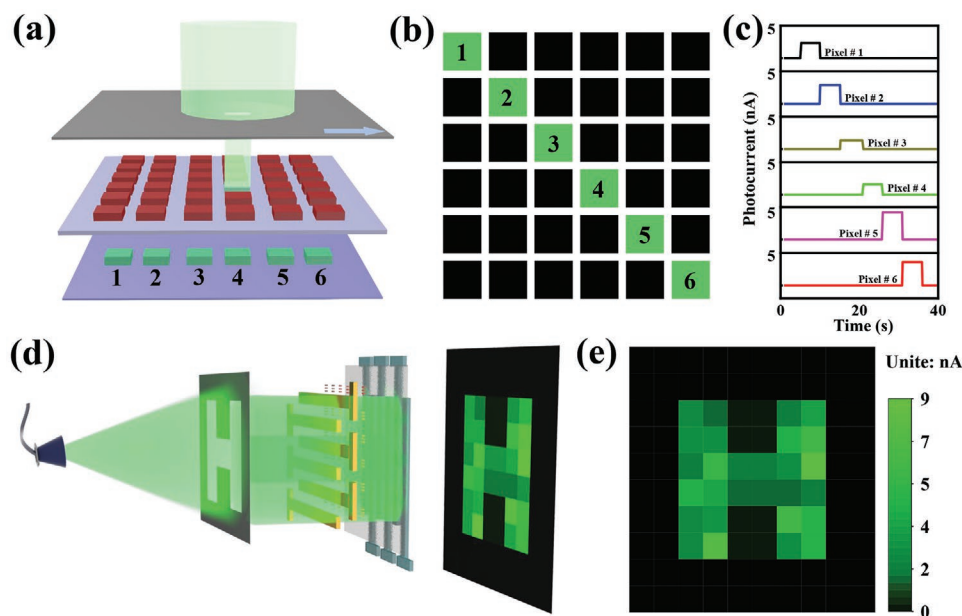
Figure 6. a) Schematic illustration of the real-time light trajectory. b) The corresponding planar graph of the trajectory. c) The change of photocurrent as the light spot went through the corresponding pixel. d) Schematic diagram of the projection imaging method. The 520 nm light is illuminated onto the device through a light-dark contrast "H" mask to form an "H" image. e) The optical image "H" of the 6 × 6 addressable photodetector arrays.

Furthermore, the device applications in light trajectory tracking and visible light imaging were also studied. As shown in **Figure 6**a, by placing a predesigned shadow mask between the light source and the PD, the device from pixel #1 to pixel #6 was independently illuminated with a moving light spot along a predesigned route. Simultaneously, the photocurrent of corresponding pixel was recorded (Figure 6b). It can be easily observed that current of the illuminated device unit increased dramatically whereas other device units remained unchanged (Figure 6c). This result demonstrates that the PDs arrays can correctly record the motion trajectory of the light spot. In addition to that, the imaging sensing capability of the 6 × 6 addressable PDs array to a simple character was also studied. Figure 6d schematically reveals the setup for measurement. The photodetectors array was projected by a homogenous visible light irradiation, before which a pre-designed shadow mask with a hollow "H" pattern was placed. Therefore, only pixel units in the area of hollow pattern could be illuminated by light irradiation whereas the others were kept in darkness. The current of all pixel units were measured dependently by corresponding row and column number and the results were showed by a 2D contrast current mapping. Obviously, as showed in Figure 6e, the shape of the "H" pattern can be clearly identified with a reasonable spatial resolution. Although this resolution is far beyond practices, it is however to improve the spatial resolution by increasing the density of the device unit and reducing the size of the device unit, which is potentially meaningful in practical applications, especially in future image sensing.

3. Conclusions

In summary, we have reported a new bottom-up method for fabrication of MAPbBr$_3$ single crystal microplate arrays with controlled spatial location and regular arrangement. Through further thermal evaporation of gold electrode on top of the microplate, 6 × 6 discrete sandwich PD arrays are successfully achieved. Optoelectronic measurement reveals that the individual pixel has excellent photoresponse with good stability at ambient atmosphere. In addition, the 36 pixels display relatively uniform photoresponse to the illuminated light, and could work effectively in light trajectory tracking and image sensing application. The as-developed method could be useful for assembly of integrated devices with more pixels which is vitally important for future optoelectronics systems.

4. Experimental Section

Materials Fabrication: 1 M MAPbBr$_3$ precursor solution was prepared through the dissolving of MABr and PbBr$_2$ (molar ratio: 1:1) into DMF. The mixture were stirred at 60 °C for 2 h at room temperature and then filtered through PTFE with pore size of 0.44 μm. The PDMS prepolymer (Dow Corning) was then mixed and the bubbles were removed in vacuum before use. The hard PDMS was prepared by casting PDMS solution against a smooth silicon mold. After baking at 60 °C for 6 h, the elastic PDMS with a thickness of about 3 mm was peeled off and cut into rectangle pieces prior to use. The MAPbBr$_3$ microplate arrays were fabricated through a modified photolithography method. First, the glass substrates were cleaned with DMF, acetone, alcohol, and deionized water sequentially. Then, a new auxiliary PMMA layer and photoresist were spin-coated on the glass substrate successively. The patterned microhole arrays were formed in the photoresist layer by photolithography and then transferred to the PMMA template through RIE at a power of 180 W for 4 min. Finally, the growth of MAPbBr$_3$ microplate arrays in the PMMA template involves the following steps: i) a certain amount of MAPbBr$_3$ precursor solution was added to the template in dropwise; ii) the PDMS was pressed against the glass substrate under a mild pressure, and the perovskite precursor solution was driven and confined into the PMMA microhole arrays; iii) the DMF evaporated slowly and the concentrated perovskite nucleated at the edge of the microhole. After about 6 h, the

PDMS was peeled off and the MAPbBr$_3$ microplate arrays were finally obtained.

Device Fabrication and Characterization: First, a patterned ITO glass with the space interval of 300 μm was rinsed with DMF, acetone, alcohol, and deionized water sequentially. Second, the microplate arrays were prepared onto the ITO electrode following the fabrication procedures of MAPbBr$_3$ mentioned above. Next, a certain amount of PMMA was spin-coated again to fill in the gap in the PMMA microhole layer. Subsequently, the RIE was employed to etch the PMMA layer slowly until the top part of the microplate exposed. Finally, the gold electrode with the spacing of 300 μm was thermal evaporated on the top surface of the microplate. The morphology and composition of the perovskite were characterized by optical microscope (MODEL MV3000) and FESEM (Quanta, FEG 250) equipped with an energy-dispersive spectrometer. The dimension of the microplates was analyzed by AFM (Dimension Icon). The crystals structure was analyzed by XRD (Rigaku D/max-rB) and HRTEM (JEM-2100F). The absorption spectrum was recorded on a Shimadzu UV–vis spectrophotometer (UV-2550). The optoelectronic characterization of the fabricated device was performed using a semiconductor characterization system (4200-SCS, Keithley) equipped with a monochromator (SP 2150, Princeton). Laser diode with wavelength of 520 nm (LP520-SF15) was used as light sources. The power intensity of all light sources was carefully calibrated using a power meter (Thorlabs GmbH., PM 100D) before measurement.

Supporting Information

Supporting Information is available from the Wiley Online Library or from the author.

Acknowledgements

Conflict of Interest

The authors declare no conflict of interest.

Data Availability Statement

Research data are not shared.

Keywords

[1] T. Leijtens, S. D. Stranks, G. E. Eperon, R. Lindblad, E. M. J. Johansson, I. J. McPherson, H. Rensmo, J. M. Ball, M. M. Lee, H. J. Snaith, *ACS Nano* **2014**, *8*, 7147.

[2] D. Shi, V. Adinolfi, R. Comin, M. J. Yuan, E. Alarousu, A. Buin, Y. Chen, S. Hoogland, A. Rothenberger, K. Katsiev, Y. Losovyj, X. Zhang, P. A. Dowben, O. F. Mohammed, E. H. Sargent, O. M. Bakr, *Science* **2015**, *347*, 519.

[3] B. Saparov, D. B. Mitzi, *Chem. Rev.* **2016**, *116*, 4558.

[4] M. A. Green, A. Ho-Baillie, H. J. Snaith, *Nat. Photonics* **2014**, *8*, 506.

[5] H. Wang, D. H. Kim, *Chem. Soc. Rev.* **2017**, *46*, 5204.

[6] H. P. Zhou, Q. Chen, G. Li, S. Luo, T. B. Song, H. S. Duan, Z. Hong, J. B. You, Y. S. Liu, Y. Yang, *Science* **2014**, *345*, 542.

[7] Z. K. Tan, R. S. Moghaddam, M. L. Lai, P. Docampo, R. Higler, F. Deschler, M. Price, A. Sadhanala, L. M. Pazos, D. Credgington, F. Hanusch, T. Bein, H. J. Snaith, R. H. Friend, *Nat. Nanotechnol.* **2014**, *9*, 687.

[8] H. M. Zhu, Y. P. Fu, F. Meng, X. X. Wu, Z. Z. Gong, Q. Ding, M. V. Gustafsson, M. T. Trinh, S. Jin, X. Y. Zhu, *Nat. Mater.* **2015**, *14*, 636.

[9] J. Yang, W. Kang, Z. Z. Liu, M. Y. Pi, L. B. Luo, C. Li, H. Lin, Z. T. Luo, J. Du, M. Zhou, X. S. Tang, *J. Phys. Chem. Lett.* **2020**, *11*, 6880.

[10] Z. X. Zhang, C. Li, Y. Lu, X. W. Tong, F. X. Liang, X. Y. Zhao, D. Wu, C. Xie, L. B. Luo, *J. Phys. Chem. Lett.* **2019**, *10*, 5343.

[11] F. X. Liang, L. Liang, X. Y. Zhao, L. B. Luo, Y. H. Liu, X. W. Tong, Z. X. Zhang, J. C. A. Huang, *Adv. Opt. Mater.* **2019**, *7*, 1801392.

[12] Z. Q. Yang, Y. H. Deng, X. W. Zhang, S. Wang, H. Z Chen, S. Yang, J. Khurgin, N. X. Fang, X. Zhang, R. M. Ma, *Adv. Mater.* **2018**, *30*, 1704333.

[13] H. Jing, R. W. Peng, R. M. Ma, J. He, Y. Zhou, Z. Q. Yang, C. Y. Li, Y. Liu, X. J Guo, Y. Y. Zhu, D. Wang, J. Su, C. Sun, W. Z Bao, M. Wang, *Nano Lett.* **2020**, *20*, 7144.

[14] S. Wang, Y. L. Liu, G. Li, J. Zhang, N. Zhang, S. M. Xiao, Q. H. Song, *Adv. Opt. Mater.* **2018**, *6*, 1701266.

[15] L. L. Gu, M. M. Tavakoli, D. Q. Zhang, Q. P. Zhang, A. Waleed, Y. Q. Xiao, K. H. Tsui, Y. J. Lin, L. Liao, J. N. Wang, Z. Y. Fan, *Adv. Mater.* **2016**, *28*, 9713.

[16] J. S. Park, J. Kyhm, H. H. Kim, S. Jeong, J. Kang, S. E. Lee, K. T. Lee, K. Park, N. Barange, J. Han, J. D. Song, W. K. Choi, I. K. Han, *Nano Lett.* **2016**, *16*, 6946.

[17] B. Jeong, H. Han, C. Park, *Adv. Mater.* **2020**, *32*, 2000597.

[18] X. J. Huang, Q. Y. Guo, D. D. Yang, X. D. Xiao, X. F. Liu, Z. G. Xia, F. J. Fan, J. R. Qiu, G. P. Dong, *Nat. Photonics* **2019**, *14*, 82.

[19] M. S. Alias, I. Dursun, D. Shi, M. I. Saidaminov, E. M. Diallo, D. Priante, T. K. Ng, O. M. Bakr, B. S. Ooi, *J. Vac. Sci. Technol. B* **2015**, *33*, 051207.

[20] J. Y. Liu, B. Shabbir, C. J. Wang, T. Wan, Q. D. Ou, P. Yu, A. Tadich, X. C. Jiao, D. W. Chu, D. C. Qi, D. B. Li, R. F. Kan, Y. M. Huang, Y. M. Dong, J. Jasieniak, Y. P. Zhang, Q. L. Bao, *Adv. Mater.* **2019**, *31*, 1901644.

[21] X. X. He, P. Liu, H. H. Zhang, Q. Liao, J. N. Yao, H. B. Fu, *Adv. Mater.* **2017**, *29*, 1604510.

[22] H. H. Zhang, Q. Liao, Y. S. Wu, Z. Y. Zhang, Q. G. Gao, P. Liu, M. L. Li, J. N. Yao, H. B. Fu, *Adv. Mater.* **2018**, *30*, 1706186.

[23] M. J. Ashley, M. N. O'Brien, K. R. Hedderick, J. A. Mason, M. B. Ross, C. A. Mirkin, *J. Am. Chem. Soc.* **2016**, *138*, 10096.

[24] A. Waleed, M. M. Tavakoli, L. L. Gu, Z. Y. Wang, D. Q. Zhang, A. Manikandan, Q. P. Zhang, R. J. Zhang, Y. L. Chueh, Z. Y. Fan, *Nano Lett.* **2017**, *17*, 523.

[25] C. H. Lin, Q. J. Zeng, E. Lafalce, S. Yu, M. J. Smith, Y. J. Yoon, Y. J. Chang, Y. Jiang, Z. Q. Lin, Z. V. Vardeny, V. V. Tsukruk, *Adv. Opt. Mater.* **2018**, *6*, 1800474.

[26] C. Zou, C. Chang, D. Sun, K. F. Bohringer, L. Y. Lin, *Nano Lett.* **2020**, *20*, 3710.

[27] J. Wu, F. J. Ye, W. Q. Yang, Z. J. Xu, D. Luo, R. Su, Y. F. Zhang, R. Zhu, Q. Gong, *Chem. Mater.* **2018**, *30*, 4590.

[28] G. Kim, S. An, S. K. Hyeong, S. K. Lee, M. Kim, N. Shin, *Chem. Mater.* **2019**, *31*, 8212.

[29] W. Deng, J. S. Jie, X. Z. Xu, Y. L. Xiao, B. Lu, X. J. Zhang, X. H. Zhang, *Adv. Mater.* **2020**, *32*, 1908340.

[30] J. Harwell, J. Burch, A. Fikouras, M. C. Gather, A. D. Falco, I. D. W. Samuel, *ACS Nano* **2019**, *13*, 3823.

[31] J. S. Zhang, Q. Guo, X. Li, C. Li, K. Wu, I. Abrahams, H. X. Yan, M. M. Knight, C. J. Humphreys, L. Su, *ACS Nano* **2020**, *14*, 11029.

[32] Y. S. Lei, Y. M. Chen, Y. Gu, C. F. Wang, Z. L. Huang, H. L. Qian, J. Y. Nie, G. Hollett, W. Choi, Y. G. Yu, N. Kim, C. Wang, T. J. Zhang, H. J. Hu, Y. X. Zhang, X. S. Li, Y. Li, W. J. Shi, Z. W. Liu, M. J. Sailor, L. Dong, Y. H. Lo, J. Luo, S. Xu, *Adv. Mater.* **2018**, *30*, 1705992.

[33] W. Jiang, H. P. Di, H. Sun, C. Zhao, F. Y. Liao, Y. Y. Zhao, *J. Cryst. Growth* **2020**, *550*, 125880.

[34] M. Zhang, F. Zhang, Y. Wang, L. J. Zhu, Y. F. Hu, Z. D. Lou, Y. B. Hou, F. Teng, *Sci. Rep.* **2018**, *8*, 11157.

[35] Z. Y. Zuo, J. X. Ding, Y. Zhao, S. J. Du, Y. F. Li, X. Y. Zhan, H. Z. Cui, *J. Phys. Chem. Lett.* **2017**, *8*, 684.

[36] Z. X. Zhang, L. H. Z, X. W. Tong, Y. Gao, C. Xie, Y. H. Tsang, L. B. Luo, Y. C. Wu, *J. Phys. Chem. Lett.* **2018**, *9*, 1185.

[37] H. C. Cheng, G. M. Wang, D. H. Li, Q. Y. He, A. X. Yin, Y. Liu, H. Wu, M. N. Ding, Y. Huang, X. Y. Duan, *Nano Lett.* **2016**, *16*, 367.

[38] F. X. Liang, J. J. Jiang, Y. Z. Zhao, Z. X. Zhang, D. Wu, L. H. Zeng, Y. H. Tsang, L. B. Luo, *Adv. Funct. Mater.* **2020**, *30*, 2001033.

[39] C. Y. Wu, J. W. Kang, B. Wang, H. N. Zhu, Z. J. Li, S. R. Chen, L. Wang, W. H. Yang, C. Xie, L. B. Luo, *J. Mater. Chem. C* **2019**, *7*, 11532.

[40] W. Y. Kong, G. A. Wu, K. Y. Wang, T. F. Zhang, Y. F. Zou, D. D. Wang, L. B. Luo, *Adv. Mater.* **2016**, *28*, 10725.

[41] X. W. Guan, W. J. Hu, M. A. Haque, N. Wei, Z. X. Liu, A. Chen, T. Wu, *Adv. Funct. Mater.* **2018**, *28*, 1704665.

[42] G. M. Wang, D. H. Li, H. C. Cheng, Y. J. Li, C. Y. Chen, A. Yin, Z. P. Zhao, Z. Y. Lin, H. Wu, Q. Y. He, M. N. Ding, Y. Liu, Y. Huang, X. F. Duan, *Sci. Adv.* **2015**, *1*, 1500613.

[43] S. X. Li, Y. S. Xu, C. L. Li, Q. Guo, G. Wang, H. Xia, H. H. Fang, L. Shen, H. B. Sun, *Adv. Mater.* **2020**, *32*, 2001998.

[44] W. Q. Wu, X. D. Wang, X. Han, Z. Yang, G. Y. Gao, Y. F. Zhang, J. F. Hu, Y. W. Tan, A. Pan, C. F. Pan, *Adv. Mater.* **2019**, *31*, 1805913.

[45] Y. C. Liu, Y. X. Zhang, K. Zhao, Z. Yang, J. S. Feng, X. Zhang, K. Wang, L. Meng, H. Ye, M. Liu, S. F. Liu, *Adv. Mater.* **2018**, *30*, 1707314.

[46] J. Xue, Z. F. Zhu, X. B. Xu, Y. Gu, S. L. Wang, L. M. Xu, Y. S. Zou, J. Z. Song, H. B. Zeng, Q. Chen, *Nano Lett.* **2018**, *18*, 7628.

[47] B. Jeong, I. Hwang, S. H. Cho, E. H. Kim, S. Cha, J. Lee, H. S. Kang, S. M. Cho, H. Choi, C. Park, *ACS Nano* **2016**, *10*, 9026.

[48] S. J. Li, H. Y. Ding, H. B. Cai, H. Zhao, Y. L. Zhao, J. L. Yang, Y. Jin, N. Pan, X. P. Wang, *J. Phys. Chem. Lett.* **2020**, *11*, 8275.